



## Hydroformylation of olefins over rhodium supported metal-organic framework catalysts of different structure



Toan Van Vu<sup>a,b</sup>, Hendrik Kosslick<sup>a,b,\*</sup>, Axel Schulz<sup>a,b,\*</sup>, Jörg Harloff<sup>a</sup>, Eckhard Paetzold<sup>b</sup>, Jörg Radnik<sup>b</sup>, Udo Kragl<sup>a,b</sup>, Gerhard Fulda<sup>c</sup>, Christoph Janiak<sup>d</sup>, Nguyen Dinh Tuyen<sup>e</sup>

<sup>a</sup> Institute for Chemistry, University of Rostock, Albert Einstein Str. 3a, D-18059 Rostock, Germany

<sup>b</sup> Leibniz-Institute for Catalysis at the University of Rostock, Albert Einstein Str. 29a, D-18059 Rostock, Germany

<sup>c</sup> Center for Electronmicroscopy, Institute of Pathology, University of Rostock, Strepel Str. 14, D-18057 Rostock, Germany

<sup>d</sup> Institute for Inorganic and Structural Chemistry, University of Düsseldorf, Universitätsstr. 1, D-40204 Düsseldorf, Germany

<sup>e</sup> Institute of Chemistry, Vietnam Academy of Science and Technology, Hanoi, Viet nam

### ARTICLE INFO

#### Article history:

Received 4 October 2012

Received in revised form 20 February 2013

Accepted 22 February 2013

Available online 6 April 2013

#### Keywords:

IRMOF-3

Metal-organic framework

Rh supported catalyst

Hydroformylation

Hierarchical pore system

### ABSTRACT

The metal-organic framework IRMOF-3 has been synthesized and functionalized with supported rhodium species. The samples have been characterized by XRD, FTIR, SEM, TEM, XPS, AAS, and nitrogen sorption measurements. It is found that originally precipitated big particles consist of hierarchically structured agglomerated nanocrystals of ca. 10–15 nm size. The big particles contain a combined macro-meso-micro pore system allowing easy access to the catalytic sites. The Rh@IRMOF-3 supported catalyst has been catalytic tested in the hydroformylation of olefins to the corresponding aldehydes. Double bond shift isomerization has been observed as side reaction. *n*-Alkenes-1 of different chain lengths and bulky or less flexible olefins as cyclohexene, 2,2,4-trimethylpentene, and hexadiene-1,5 have been studied. The Rh@IRMOF-3 catalyst shows high activity and selectivity to *n*-aldehydes in the hydroformylation of linear alkene-1. The comparison of catalytic data obtained with the hydroformylation of *n*-hexene-1 over the different rhodium loaded MOFs as MOF-5, MIL-77, and MIL-101 show a significant influence of the MOF-structure on the catalytic properties.

© 2013 Elsevier Inc. All rights reserved.

### 1. Introduction

Porous metal-organic frameworks (MOFs) are well-known crystalline inorganic-organic hybrid materials, in which metal clusters and organic ligands are connected in space in order to form three-dimensional ordered frameworks. These materials possess a variety of properties such as high specific surface area and pore volume, tunable pore size, and an organic-inorganic hybrid character with a strictly alternating arrangement of organic linkers and metal oxide sites. The huge amount of possibilities to functionalize the MOF by exchange of organic linkers and metal compartments allow to vary the material properties to a large extent [1–8]. The outstanding properties of MOFs make them interesting for the application in gas storage, separation, catalysis, and others [9–14]. Therefore, MOFs attracted attention for use as catalyst or catalytic support. IRMOF-3 is an amino-functionalized MOF, which is isostructural with MOF-5. It is an interesting material for the

application as catalytic support for rhodium in the hydroformylation of olefins.

Discovered by Otto Roelen in 1938 [15], the hydroformylation is the reaction of olefinic double bonds with synthesis gas yielding linear and branched aldehydes as primary products. Linear aldehydes, which are more valuable than branched aldehydes, can be used for the production of alcohols. Approximately, 9 million metric tons of aldehydes and alcohols are annually produced using this reaction [16]. These products are important feed stocks for the synthesis of plasticizers, detergents, adhesives, solvents, pharmaceuticals, and agrochemicals as well [17,18].

Even though the traditional use of cobalt or rhodium complexes as homogeneous catalysts in industrial hydroformylation is effective, the homogeneous process suffers from problems of catalyst recovery. Therefore, many efforts have been undertaken to immobilize these catalysts on supports as silica, alumina, micro and mesoporous materials like zeolites and MCM-41, activated carbons, and organic polymers [19–32]. However, it is still a challenge due to the loss of activity [16]. Porous metal-organic frameworks give new opportunities for the heterogenization of homogeneous catalysts. The hybrid nature with defined separated and strictly alternatively arranged inorganic units (metal oxides) and organic linkers should allow a high dispersion of active metal species of

\* Corresponding authors. Address: Institute for Chemistry, University of Rostock, Albert Einstein Str. 3a, D-18059 Rostock, Germany. Tel.: +49 381 498 6384; fax: +49 381 498 6382.

E-mail addresses: [hendrik.kosslick@uni-rostock.de](mailto:hendrik.kosslick@uni-rostock.de) (H. Kosslick), [axel.schulz@uni-rostock.de](mailto:axel.schulz@uni-rostock.de) (A. Schulz).

unique structure in a single site manner throughout the MOF framework. High porosity and large pore openings may enhance the mass transfer properties. Both are expected to improve the catalytic performance.

This study deals with the preparation, characterization, and testing of the rhodium supported metal-organic framework IRMOF-3 catalyst without addition of further ligands. The catalyst activity is compared with MOFs of other pore sizes. The aim is to check the catalytic performance of the rhodium supported MOF catalyst in the hydroformylation reaction.

## 2. Experiment

### 2.1. Materials

IRMOF-3 was solvothermally synthesized by an optimized procedure based on literature [33,34]. The starting materials included  $\text{H}_2\text{NC}_6\text{H}_3\text{-1,4-(COOH)}_2$  (2-aminoterephthalic acid) and  $\text{Zn}(\text{NO}_3)_2$  (zinc nitrate). DEF (diethylformamide) was used as solvent. Prior to use, the DEF was distilled and dried over calcium hydride.

In detail, 2.537 g (~14 mmol) of  $\text{H}_2\text{NC}_6\text{H}_3\text{-1,4-(COOH)}_2$  (Sigma-Aldrich) and 11.003 g (~42 mmol) of  $\text{Zn}(\text{NO}_3)_2 \cdot 4\text{H}_2\text{O}$  (Merck) were dissolved in 350 mL of DEF (Sigma-Aldrich) in a glass reactor which was equipped with a dry tube on the top filled with calcium hydride. The reaction mixture was heated to 105 °C under stirring. Then it was allowed to crystallize at 105 °C for 24 h under static condition. The following work up was carried out under argon atmosphere and use of dried solvents to obtain pure IRMOF-3.

The crystallized product was filtered off and washed three times with 10 mL of  $\text{CH}_2\text{Cl}_2$  (dichloromethane). The resulting solid was suspended in 50 mL of DEF and heated under refluxing at 130 °C for 1 h. The solid was filtered off and washed again with  $3 \times 10$  mL of  $\text{CH}_2\text{Cl}_2$ . Next, it was given into 50 mL of  $\text{CH}_2\text{Cl}_2$ , slightly shaken, and allowed to stay overnight at room temperature. The solid was again filtered off and the above mentioned procedure was repeated twice in order to remove non-reacted aminoterephthalic acid and the low volatile DEF solvent from the synthesis product. Finally, the product was dried at 105 °C under vacuum to obtain the as-synthesized IRMOF-3. The small and large porous metal-organic frameworks, MIL-77 and MIL-101, were synthesized according to procedures given in Refs. [35,36].

For rhodium loading onto the support under argon atmosphere, 10 mg of  $\text{Rh}(\text{acac})(\text{cod})$  [(acetylacetonato)(cycloocta-1,5-diene)rhodium(I)] were poured into a beaker glass containing 28 mL of acetonitrile (Baker) and 20 mL of toluene (Merck) under stirring. A clear pale yellow solution was formed. Then 4 g of the as-synthesized IRMOF-3 were added under slight stirring. The suspension was slowly heated to ca. 70 °C to evaporate the solvents. The obtained product was washed three times with 5 mL of toluene and dried at 70 °C under vacuum. The resulting Rh@IRMOF-3 catalyst was used for catalytic testing.

### 2.2. Characterization

The IRMOF-3 and Rh@IRMOF-3 were characterized in detail by XRD, FTIR, SEM, TEM, XPS, AAS, and nitrogen sorption measurements. The XRD measurements were carried out on the STADI-P (STOE) X-ray diffractometer using monochromatic  $\text{CuK}\alpha$  radiation ( $\lambda = 1.5418 \text{ \AA}$ ). SEM images were recorded on the DSM 960A electron microscope operating at 10.0 kV (Carl Zeiss, Oberkochen) with a resolution of 4 nm. The samples were placed on sample plates and coated with a very thin layer of gold by using a plasma distribution method. The base vacuum of the chamber was ca.  $2 \times 10^{-5}$  kPa. TEM measurements were carried out with a LIBRA 120 electron microscope (Carl Zeiss, Oberkochen) at 120 kV with a res-

olution of 0.35 nm. Images were recorded with a digital camera with  $2000 \times 2000$  pixels. IR spectroscopic measurements were performed on a Nicolet 380 FTIR spectrometer coupled with smart orbit ATR device with a resolution of  $4 \text{ cm}^{-1}$ . XPS measurements were done at an ESCALAB220iXL spectrometer (Thermo Fisher) with monochromatic  $\text{AlK}\alpha$  radiation ( $E = 1486.6 \text{ eV}$ ). The samples were fixed on a stainless steel sample holder with double adhesive carbon tape. The binding energies were referred to  $\text{C}_{1s}$  at 284.8 eV. For determination of the binding energy and peak area the peak were fitted with Gaussian-Lorentzian curves. The base pressure of the UHV chamber was below  $1 \times 10^{-7}$  Pa. Nitrogen adsorption measurements were performed on an ASAP 2010 sorption system. Before measurements, the samples were dried by heating at 150 °C under reduced pressure. Nitrogen adsorption measurements were carried out at -196 °C. The rhodium content was determined by atomic absorption spectrometry with an AAS-Analyst 300 device (Perkin Elmer). A nitrous oxide/acetylene or air/acetylene mixture was used for the burner system.

### 2.3. Catalysis

Linear alkene-1 substrates with 6–12 carbon atoms such as *n*-hexene-1 ( $\geq 97\%$ , Aldrich), *n*-octene-1 ( $\geq 98\%$ , Aldrich), *n*-decene-1 ( $\geq 95\%$ , Acros), and *n*-dodecene-1 (93–95%, Acros) were used to investigate the catalytic performance of Rh@IRMOF-3 in the hydroformylation of olefins in more detail. Additionally, some bulky or less reactive olefins as cyclohexene ( $\geq 99\%$ , Sigma-Aldrich), 2,4,4-trimethylpentene ( $\geq 99\%$ , Sigma-Aldrich), and hexadiene-1,5 were involved in the study. For comparison, rhodium loaded MIL-77 and MIL-101 were tested in the hydroformylation of *n*-hexene-1.

All hydroformylation experiments were carried out in a 100 mL PARR reactor at 100 °C and 50 bar ( $\text{CO}/\text{H}_2 = 1$ ) under stirring at ca. 1000 rpm. Toluene was used as solvent. Typically, for *n*-hexene-1 hydroformylation, 95 mg of Rh@IRMOF-3, 12.5 mL of *n*-hexene-1, and 30 mL of toluene were loaded into the reactor. The *n*-hexene-1 to catalyst molar ratio based on rhodium was ca. 100,000/1. After loading, the reactor was evacuated and purged with argon. The procedure was repeated in order to remove air and residual moisture. Thereafter, the reactor was immediately loaded with synthesis gas up to a pressure of 50 bar at room temperature. Finally, the reaction mixture was heated under stirring at ca. 1000 rpm and maintained at a temperature of 100 °C during the course of reaction. The reactor was equipped with a gas introduction stirrer. The reactions of the other olefins were carried out in the same way. The molar olefin/Rh ratio was kept constant.

## 3. Results and discussion

### 3.1. Characterization

The X-ray diffraction patterns of the as-synthesized IRMOF-3 and the used Rh@IRMOF-3 catalyst are shown in Fig. 1. The reflections are well resolved and the observed patterns correspond to the structure of IRMOF-3 [34]. The similarity of XRD patterns obtained for the as-synthesized and the used rhodium loaded material indicates that the structure of the MOF framework is maintained after Rh loading and even catalytic testing. The FTIR spectra of the as-synthesized form and the supported catalyst are shown in Fig. 2. They are very well resolved and show the typical vibration bands observed with benzene carboxylate present as a linker. The absorbances observed between  $1600\text{--}1330 \text{ cm}^{-1}$  and  $830\text{--}750 \text{ cm}^{-1}$  are related to the vibrations of the carboxyl and the amino substituted phenyl groups. The very strong vibration band located at ca.  $1255 \text{ cm}^{-1}$  in both samples are assigned to the C–N stretch vibrations of amino groups attached to the

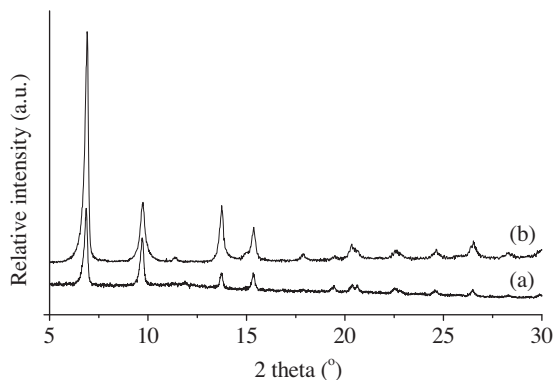


Fig. 1. XRD patterns of (a) IRMOF-3 and (b) the used Rh@IRMOF-3 catalyst.

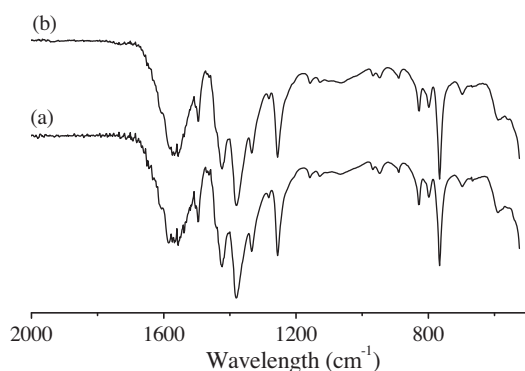


Fig. 2. FTIR spectra of (a) IRMOF-3 and (b) Rh@IRMOF-3.

benzene ring. The spectra of the as-synthesized material and the rhodium loaded form are quite similar.

The SEM/TEM images of IRMOF-3 and the Rh-loaded material are shown in Figs. 3–5 in different magnification.

The starting material consists of large block- and cube-shaped particles of *ca.* 150–350 μm size. They show well-shaped and smooth faces. However, they are easily broken into compartments during handling. The big particles show cracks (Fig. 3a and b). The high magnification image shows, however, that these large particles do not represent single crystals. They consist of agglomerates of much smaller, *ca.* 0.5 μm, particles (Fig. 4a). Interestingly, the TEM image shows that these particles are composed of nanoparticles of *ca.* 10–15 nm size (Fig. 4b). The big, close to mm-sized, as-synthesized IRMOF-3 particles consist of agglomerated small nanoparticles, which are hierarchically assembled (10 nm → 0.5 μm → 300 μm), into large size compartments.

After rhodium loading, which is connected with heating and stirring of the sample followed by evaporation of the solvent, the particles show some damage. The former particles are broken into compartments of irregular shapes (Fig. 5a). The faces of the particles are rough. Their edges and corners are more rounded. The particles show cracks and slits (Fig. 5b).

The nitrogen adsorption–desorption isotherms of the IRMOF-3 and its Rh loaded form are shown in Fig. 6. At low relative pressure of up to  $p/p_0 = 0.01$ , the extremely steep increase of the isotherm indicates the filling of the micropores. The enhancement of the nitrogen uptake between a relative pressure of  $p/p_0 = 0.01$ –0.2 shows the filling of the open pores of the MOF. The isotherm of Rh@IRMOF-3 shows a similar appearance. The BET surface area of the starting material amounts to *ca.* 2450 m<sup>2</sup>/g and the specific pore volume to *ca.* 0.96 cm<sup>3</sup>/g showing high crystallinity and

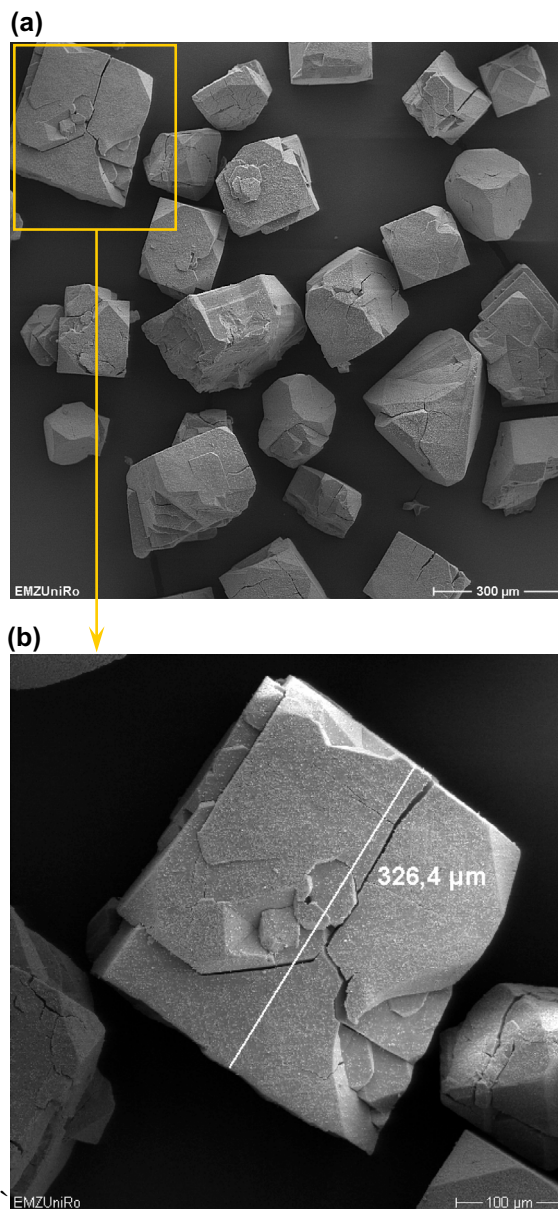
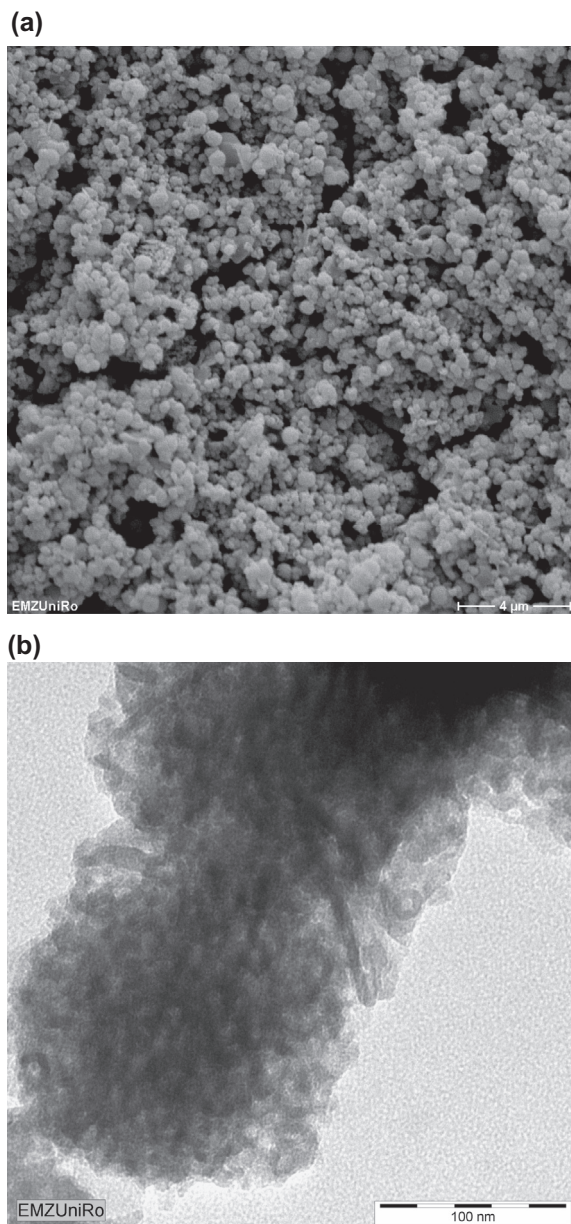


Fig. 3. SEM images of IRMOF-3 in different magnification. (a) Block- and cube-shaped particles, and (b) a large particle with smooth faces and cracks.

porosity of IRMOF-3. After rhodium loading, the BET surface area and specific pore volume markedly decrease to *ca.* 1874 m<sup>2</sup>/g and *ca.* 0.73 cm<sup>3</sup>/g, respectively, indicating partial crystal damage. Also a second desorption step at  $p/p_0 = 0.5$  is observed in the isotherm indicating the presence of textural mesopores of *ca.* 4 nm size that could improve the accessibility of the pore system of the Rh@IRMOF-3. Also the starting material contains already such mesopores but to a much lower extent. The shape of the hysteresis loop of the isotherm is consistent with the presence of slit-like pores. The loop is flat and the curves are parallel indicating parallel pore walls [37,38]. Also the formation of ink-bottle neck pores cannot be excluded which give rise to a similar hysteresis loop [39]. The loss of porosity and the occurrence of the textural properties after rhodium loading are in agreement with SEM results.

In the XPS spectrum of IRMOF-3, a Zn<sub>2p</sub> signal (doublet) appears at 1023.98 and 1047.08 eV. The peaks are asymmetric. Also a single asymmetric O<sub>1s</sub> peak appears at 532.93 eV. Even the N<sub>1s</sub> peak at 399.27 eV is highly asymmetric. Only the C<sub>1s</sub> peak is split into



**Fig. 4.** SEM and TEM images of IRMOF-3. (a) High magnification SEM image of a big particle showing high textural porosity and hierarchically arranged  $\mu\text{m}$ -sized particles, and (b) TEM image showing agglomerated nanoparticles forming the  $\mu\text{m}$ -sized particles.

two components located at 284.8 eV and 288.52 eV. Additionally, a shoulder arises at *ca.* 293 eV. Rhodium loading has a severe impact on the appearance and location of the  $\text{Zn}_{2p}$ ,  $\text{O}_{1s}$ , and  $\text{C}_{1s}$  XPS signals, respectively, although the loading is rather low. According to the AAS analysis, the sample contains only 0.11 wt.% of rhodium. This points to a strong interaction between the Rh and the MOF lattice indicating that the Rh is located in the pores of the MOF and highly dispersed. Largest shifts to lower energy are observed with the  $\text{Zn}_{2p}$  and the  $\text{O}_{1s}$  signals of the metal oxide sites (Table 1). The latter signal is significantly broadened.

The  $\text{N}_{1s}$  signal is split into two components (Fig. 7). A rhodium signal could not be unambiguously identified in the XPS. However, the marked changes observed after rhodium loading indirectly confirms the presence of the rhodium in the pore structure probably close to the metal oxide sites.

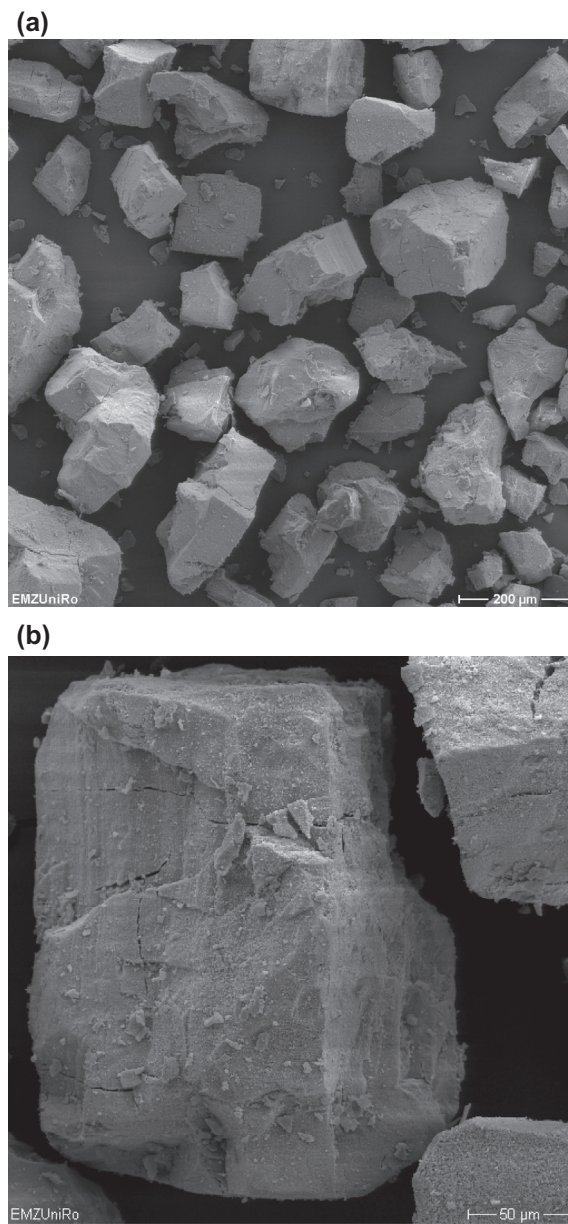


**Fig. 5.** SEM images of Rh@IRMOF-3 in different magnification. (a) Overview showing irregular sized large particles, and (b) A selected big cubical particle showing rough faces and cracks/splits.

Finally, it is concluded that the catalytic material consists of agglomerated small IRMOF-3 nanocrystals. A high textural porosity of the catalytic material is achieved by hierarchically assembling of IRMOF-3 nanocrystals into 0.5  $\mu\text{m}$  sized particles forming finally close to mm scale particles (up to *ca.* 330  $\mu\text{m}$ ). Thereby, a combined micro – meso – macro pore system is formed (Fig. 4). As a result, the catalytic sites are highly accessible.

### 3.2. Catalysis

*n*-Alkene-1 molecules with varied chain lengths have been used to investigate the catalytic behavior of Rh@IRMOF-3 in the hydroformylation of olefins. The olefins are converted to the corresponding *n*- and *i*-aldehydes as preferred products. Also the formation of double bond shifted *i*-alkenes is observed.

The total conversions of the different *n*-alkene-1 substrates in the hydroformylation over Rh@IRMOF-3 are shown in Fig. 8. As

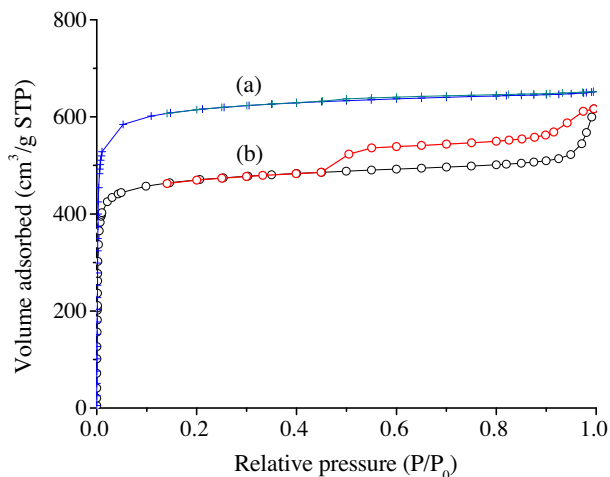


**Fig. 6.** Nitrogen adsorption isotherms of (a) IRMOF-3 on the top and (b) Rh@IRMOF-3 on the bottom.

**Table 1**  
Electron binding energy of elements of IRMOF-3 before and after loading rhodium species.

Peak	Binding energy (eV)	
	IRMOF-3	Rh@IRMOF-3
N <sub>1s</sub>	399.27	398.23
		401.00
C <sub>1s</sub>	284.80	281.15
	288.52	284.80
		288.73
O <sub>1s</sub>	532.93	529.60
		531.14
Zn <sub>2p</sub>	1023.98 (1/1)	1019.47 (1/1)
	1047.08 (1/2)	1021.92 (2/1)
		1042.72 (1/2)
		1045.03 (2/2)

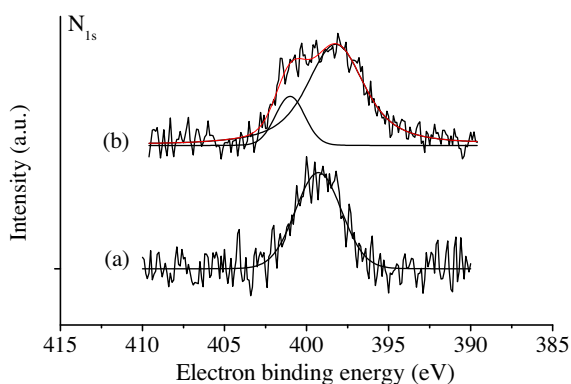


**Fig. 7.** XPS N<sub>1s</sub> spectra of (a) IRMOF-3 on the bottom and (b) Rh@IRMOF-3 on the top showing a splitted signal.

revealed, the reaction proceeds very fast in the first 1–2 h. The total conversion nearly linearly increases with reaction time. After 1 h of reaction, the conversions of *n*-hexene-1, *n*-decene-1, and *n*-dodecene-1 achieve *ca.* 30–45%. In contrast, *n*-octene-1 shows a distinct lower conversion of only 5%. After 3 h of reaction, conversions of more than 90% are achieved for all *n*-alkene-1 used (Fig. 8). The low activity of the *n*-octene-1 is explained by limited access to

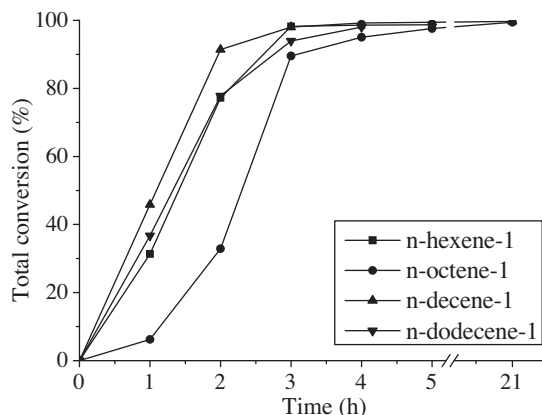


**Fig. 8.** Total conversion of *n*-alkene-1 in the hydroformylation over Rh@IRMOF-3 catalyst at  $T = 100\text{ }^{\circ}\text{C}$ ,  $P = 50\text{ bar}$ .

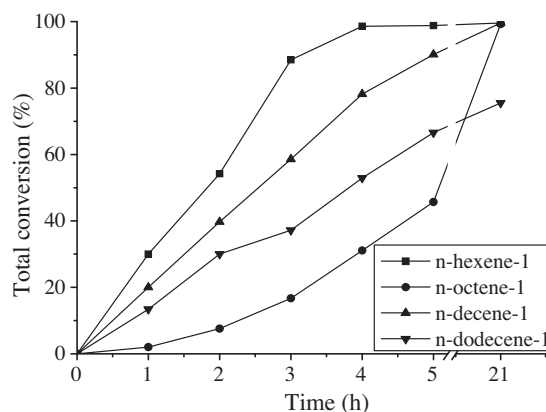


**Fig. 9.** Total conversion of *n*-alkene-1 in the hydroformylation over Rh@MOF-5 catalyst at  $T = 100\text{ }^{\circ}\text{C}$ ,  $P = 50\text{ bar}$ .

the active Rh sites. Although located in the open pore structure, the more linear shaped long-tailed *n*-octene-1 molecule, with a chain length of *ca.* 10 Å, is difficult to arrange with its double bond at the active site in the confined space of the pore cages. A similar effect is found with rhodium supported MOF-5 (Fig. 9).

The selectivities to aldehydes are nearly unchanged during the first 3 h of reaction and vary between 26% and 32% depending on the substrate (Fig. 10). They are lowest for the *n*-octene-1. They further increase after prolonged reaction time due to the hydroformylation of double bond shifted *i*-alkenes. The corresponding aldehyde yields are shown in Fig. 11. They increase especially in the first 3 h of reaction and with prolonged reaction time in line with the course of conversion and aldehyde selectivity, respectively.

The *n*/*i*-aldehyde ratio varies between *ca.* 2.7 and 3 in the first 2 h of reaction (Fig. 12). The *n*/*i*-ratio decreases with further reaction time. The total conversion has been nearly reached at this stage. Only double bond shifted olefins remain in the reaction solution. Their hydroformylation leads to a decrease of the *n*/*i*-ratio during prolonged reaction time. In the case of *n*-octene-1, unreacted *n*-octene-1 is still present in the reaction mixture maintaining the higher *n*/*i*-ratio for longer time. In the case of the more bulky cyclohexene and the double bond shielded 2,2,4-trimethylpentene, the conversion to aldehydes is lower than that of *n*-olefins and reaches *ca.* 20% after 2 h. In contrast, the steric demanding, less flexible hexadiene-1,5 is not converted. The approach of the C=C double bond to the active rhodium sites is prohibited (Fig. 13).

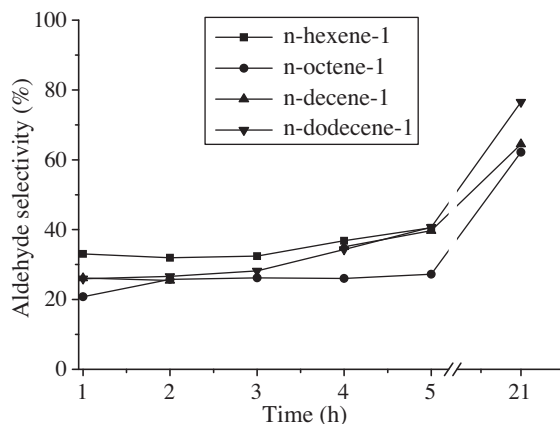


Fig. 10. The selectivity to aldehydes in the hydroformylation of *n*-alkene-1 over Rh@IRMOF-3 catalyst at  $T = 100\text{ }^{\circ}\text{C}$ ,  $P = 50\text{ bar}$ .

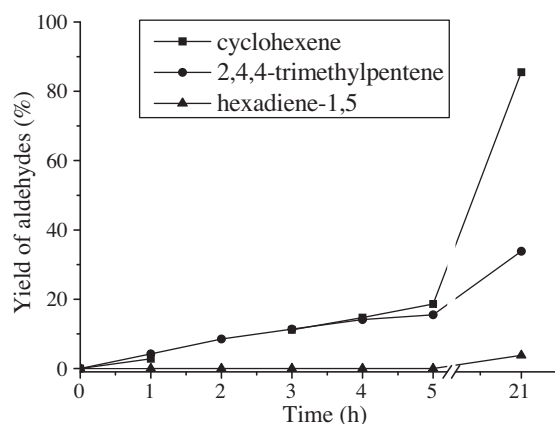


Fig. 13. Yield of aldehydes in the hydroformylation of bulky or stiff olefins over Rh@IRMOF-3 catalyst at  $T = 100\text{ }^{\circ}\text{C}$ ,  $P = 50\text{ bar}$ .

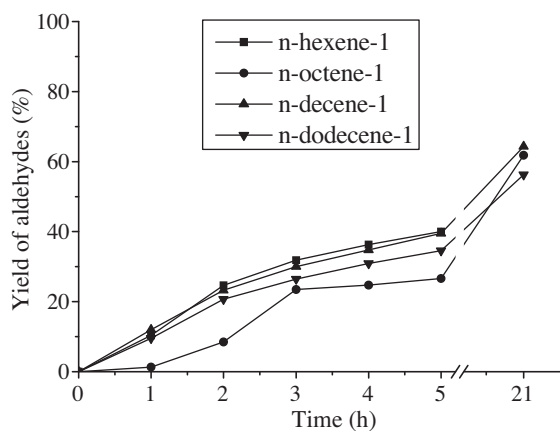


Fig. 11. Yield of aldehydes in the hydroformylation of *n*-alkene-1 over Rh@IRMOF-3 catalyst at  $T = 100\text{ }^{\circ}\text{C}$ ,  $P = 50\text{ bar}$ .

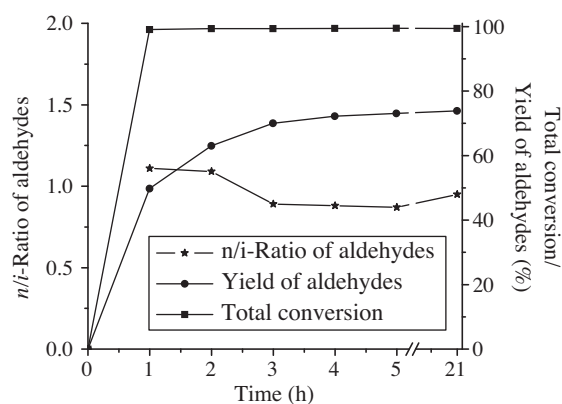


Fig. 14. Total conversion and yield of aldehydes in the hydroformylation of *n*-hexene-1 over Rh@MIL-77 catalyst at  $T = 100\text{ }^{\circ}\text{C}$ ,  $P = 50\text{ bar}$ .

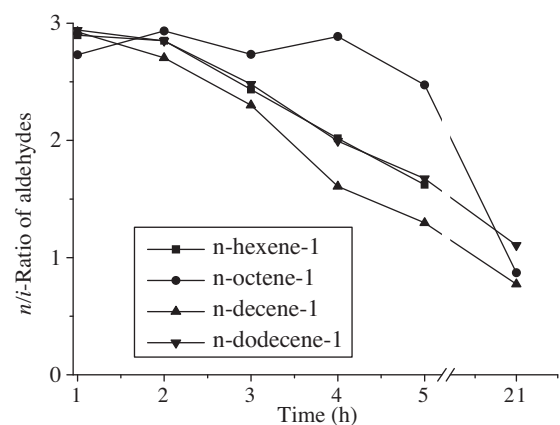


Fig. 12. *n/i*-Ratio of aldehydes in the hydroformylation of *n*-alkene-1 over Rh@IRMOF-3 catalyst at  $T = 100\text{ }^{\circ}\text{C}$ ,  $P = 50\text{ bar}$ .

The IRMOF-3 catalyst has been reused after filtration without further work up. It is found that the catalytic activity is decreased. However, the selectivity behavior, characterized by the *n/i*-aldehyde ratio, remains unchanged.

Additionally, the small pore rhodium supported metal-organic framework MIL-77 has been tested using *n*-hexene-1 in order to

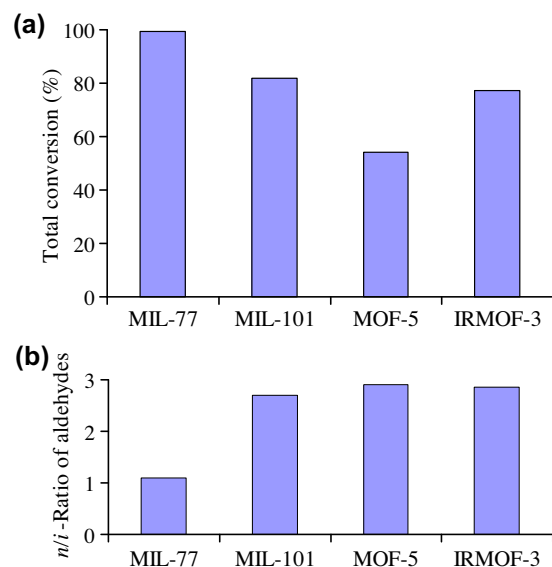


Fig. 15. (a) Total conversion and (b) *n/i*-Ratio of aldehydes in the hydroformylation of *n*-hexene-1 over different Rh@MOF catalysts after 2 h of reaction at  $T = 100\text{ }^{\circ}\text{C}$ ,  $P = 50\text{ bar}$ .

**Table 2**  
Porosity and BET surface areas of used MOF supports [1,2,35,41].

MOFs	Formula	Free pore diameter (Å)	Free aperture for window (Å)	BET surface area (m <sup>2</sup> /g)
MIL-77	Ni <sub>2</sub> 0[(MGLA) <sub>2</sub> 0(H <sub>2</sub> O) <sub>8</sub> ]-33H <sub>2</sub> O	–	–	313
MIL-101	Cr <sub>3</sub> F(H <sub>2</sub> O) <sub>2</sub> O(BDC) <sub>3</sub> ·25H <sub>2</sub> O	29–34	12–14.7	4703
MOF-5	Zn <sub>4</sub> O(BDC) <sub>3</sub>	12	8	2337
IRMOF-3	Zn <sub>4</sub> O(BDC-NH <sub>2</sub> ) <sub>3</sub>	12	<8	2450

BDC – [(O<sub>2</sub>C)–C<sub>6</sub>H<sub>4</sub>–(CO<sub>2</sub>)], benzene dicarboxylate; MGLA – [(C<sub>6</sub>H<sub>8</sub>O<sub>4</sub>)], 3-methylglutarate.

check the catalytic performance of the rhodium species exposed to the reaction solution. The olefins have hardly access to the small pores and internal rhodium sites. Therefore, the reaction should take place mainly at the external surface. The results show that the *n*-hexene-1 is immediately converted after very short reaction time of <1 h. This points to the high dispersion of the rhodium active species on the crystal surface. The selectivity to aldehydes is high and increases from 50% at the beginning to ca. 72% after prolonged reaction time (Fig. 14) due to the conversion of double bond shifted *i*-alkenes to the corresponding aldehydes. As a result, the *n*/*i*-ratio decreases. With a *n*/*i*-aldehyde ratio of ca. 1.1–0.9, the selectivity to *n*-aldehyde of Rh@MIL-77 is comparatively low. These results, the high activity and selectivity to aldehydes but low *n*/*i*-aldehyde ratio, point to a location of active sites at the external surface. The lower activity (shown by total conversion), but distinctly higher selectivity to *n*-aldehyde found with Rh@IRMOF-3, indicates that the active sites are located inside the pores. With MIL-101, high conversion of *n*-hexene-1 is found after 2 h of reaction. This finding is in line with the very large pore sizes and high porosity of this material. The selectivity to aldehydes and the *n*/*i*-ratio is similar to the other porous MOFs (Fig. 15).

### 3.3. Comparison of different MOFs

Compared to IRMOF-3, the catalytic activity of Rh/MOF-5 [40] is lower, although the window size is somewhat larger (Table 2). In contrast to MOF-5, the terephthalate linker in IRMOF-3 is substituted by a space demanding amino group. Also the differences in the conversions obtained with olefins of different chain length are larger with the Rh@MOF-5 catalyst (Fig. 9). As shown above, the IRMOF-3 catalyst consists of small nanoparticles of ca. 10–15 nm size, which are easy accessible via a hierarchically structured macro – meso pore system in between the nanoparticles. Additionally, the diffusion pathway of the molecule in the catalyst is substantially reduced due to the small size of the nanoparticles, which corresponds to ca. 4–6 unit cell lengths,  $a_0 = 2.57$  nm [42,43] or 8–12 cages. Both lead to the improvement of the mass transfer of the molecules in the catalyst compared to the more open MOF-5 structure and, hence, to an enhancement of the conversion. Therefore, the influence of the chain length of the olefin is less pronounced with IRMOF-3 than with MOF-5 (Fig. 9). The latter is best reflected in the very low conversion of the *n*-octene-1 over Rh@MOF-5 at short reaction time. On the other hand, the selectivity to *n*-aldehydes is similar for both structure types. This finding confirms that the active rhodium species are located in the pores of the catalyst. In case of location of active sites outside of the pore system on the external surface of the catalyst, the *n*/*i*-aldehyde ratio is markedly diminished to ca. 1.1–0.9 as shown with Rh@MIL-77 (Figs. 14 and 15). Also the conversion found with external sites of MIL-77 is markedly higher due to the reduced mass transfer resistance. The findings with MIL-101 are in line with the expectation. The large porous framework reduces mass transfer limitations compared to the smaller pores of MOF-5 leading to high conversion of the *n*-hexene-1 (Fig. 15). On the other hand, selectivity to aldehydes and *n*/*i*-aldehyde ratio are similar to those found with the

other open porous MOF structures under consideration. In summary, presented catalytic findings confirm that the MOF structure has a significant impact on the catalytic properties.

## 4. Conclusion

The rhodium supported IRMOF-3 catalyst has been synthesized. The big, close to mm-sized, as-synthesized IRMOF-3 particles are constructed of hierarchically arranged small primary MOF nanocrystals and secondary microparticles forming a combined micro-meso-macro pore system allowing easy access to active sites. The catalyst is highly active in the hydroformylation of olefins. High selectivity to linear *n*-aldehydes has been achieved. The comparison with other Rh@MOF catalysts based on MOF-5, MIL-77, and MIL-101 shows that the catalytic performance is markedly influenced by the MOF structure.

## Acknowledgement

This work was partially supported by the German Academic Exchange Service (DAAD) and granted by the Ministry of Education and Training of Vietnam (MOET) which is gratefully acknowledged.

## References

- [1] O.M. Yaghi, M. O'Keeffe, N.W. Ockwig, H.K. Chae, M. Eddaoudi, J. Kim, *Nature* 423 (2003) 705–714.
- [2] G. Férey, C. Mellot-Draznieks, C. Serre, F. Millange, J. Dutour, S. Surblé, I. Margiolaki, *Science* 309 (2005) 2040–2042.
- [3] M. Dogru, A. Sonnauer, A. Gavryushin, P. Knochel, T. Bein, *Chem. Commun.* 47 (2011) 1707–1709.
- [4] S. Hermes, M.-K. Schröter, R. Schmid, L. Khodeir, M. Muhler, A. Tissler, R.W. Fischer, R.A. Fischer, *Angew. Chem. Int. Ed.* 44 (2005) 6237–6241.
- [5] M.-H. Cha, M.C. Nguyen, Y.-L. Lee, J. Im, J. Ihm, *J. Phys. Chem. C* 114 (2010) 14276–14280.
- [6] S.M. Cohen, *Chem. Rev.* 112 (2011) 970–1000.
- [7] P. Falcaro, A.J. Hill, K.M. Nairn, J. Jasieniak, J.I. Mardel, T.J. Bastow, S.C. Mayo, M. Gimona, D. Gomez, H.J. Whitfield, R. Riccò, A. Patelli, B. Marmiroli, H. Amenitsch, T. Colson, L. Villanova, D. Buso, *Nat. Commun.* 2 (2011) 237.
- [8] O. Shekha, H.K. Arslan, K. Chen, M. Schmittel, R. Maul, W. Wenzel, C. Woll, *Chem. Commun.* 47 (2011) 11210–11212.
- [9] S. Opelt, S. Türk, E. Dietzsch, A. Henschel, S. Kaskel, E. Klemm, *Catal. Commun.* 9 (2008) 1286–1290.
- [10] M. Eddaoudi, J. Kim, N. Rosi, D. Vodak, J. Wachter, M. O'Keeffe, O.M. Yaghi, *Science* 295 (2002) 469–472.
- [11] R.J. Kuppler, D.J. Timmons, Q.-R. Fang, J.-R. Li, T.A. Makal, M.D. Young, D. Yuan, D. Zhao, W. Zhuang, H.-C. Zhou, *Coord. Chem. Rev.* 253 (2009) 3042–3066.
- [12] A. Henschel, K. Gedrich, R. Kraehnert, S. Kaskel, *Chem. Commun.* (2008) 4192–4194.
- [13] I. Luz, F.X. Llabrés i Xamena, A. Corma, *J. Catal.* 276 (2010) 134–140.
- [14] C. Sanchez, K.J. Shea, S. Kitagawa, *Chem. Soc. Rev.* 40 (2011).
- [15] B. Cornils, W.A. Herrmann, M. Rasch, *Angew. Chem. Int. Ed.* 33 (1994) 2144–2163.
- [16] S.K. Sharma, P.A. Parikh, R.V. Jasra, *J. Mol. Catal. A* 316 (2010) 153–162.
- [17] H.-W. Bohnen, B. Cornils, in: B.C. Gates, H. Knözinger (Eds.), *Advances in Catalysis*, vol. 47, Academic Press, 2002, pp. 1–64.
- [18] C.D. Frohning, C.W. Kohlpaintner, H.-W. Bohnen, *Applied Homogeneous Catalytic with Organometallic Compounds – A Comprehensive Handbook in Three Volumes*, second ed., Wiley-VCH, 2002.
- [19] D.E. Bryant, M. Kilner, *J. Mol. Catal. A* 193 (2003) 83–88.
- [20] K.-C. Song, J.Y. Baek, J.A. Bae, J.-H. Yim, Y.S. Ko, D.H. Kim, Y.-K. Park, J.-K. Jeon, *Catal. Today* 164 (2011) 561–565.
- [21] D. Cauzzi, M. Lanfranchi, G. Marzolini, G. Predieri, A. Tiripicchio, M. Costa, R. Zanoni, *J. Organomet. Chem.* 488 (1995) 115–125.

- [22] J.A. Bae, K.-C. Song, J.-K. Jeon, Y.S. Ko, Y.-K. Park, J.-H. Yim, *Microporous Mesoporous Mater.* 123 (2009) 289–297.
- [23] J. Balu e, J.C. Bay on, *J. Mol. Catal. A* 137 (1999) 193–203.
- [24] U. Ferenc, *Coord. Chem. Rev.* 251 (2007) 2087–2102.
- [25] H. Zhu, Y. Ding, H. Yin, L. Yan, J. Xiong, Y. Lu, H. Luo, L. Lin, *Appl. Catal., A* 245 (2003) 111–117.
- [26] Y. Zhang, H.-B. Zhang, G.-D. Lin, P. Chen, Y.-Z. Yuan, K.R. Tsai, *Appl. Catal., A* 187 (1999) 213–224.
- [27] T.A. Zeelie, A. Root, A.O.I. Krause, *Appl. Catal., A* 285 (2005) 96–109.
- [28] T.-J. Yoon, J.I. Kim, J.-K. Lee, *Inorg. Chim. Acta.* 345 (2003) 228–234.
- [29] L. Yan, Y.J. Ding, L.W. Lin, H.J. Zhu, H.M. Yin, X.M. Li, Y. Lu, *J. Mol. Catal. A* 300 (2009) 116–120.
- [30] J. Wrzyszczyk, M. Zawadzki, A.M. Trzeciak, J.J. Zi lkowski, *J. Mol. Catal. A* 189 (2002) 203–210.
- [31] A. Riisager, P. Wasserscheid, R. van Hal, R. Fehrmann, *J. Catal.* 219 (2003) 452–455.
- [32] K. Mukhopadhyay, R.V. Chaudhari, *J. Catal.* 213 (2003) 73–77.
- [33] S.S. Kaye, A. Dailly, O.M. Yaghi, J.R. Long, *J. Am. Chem. Soc.* 129 (2007) 14176–14177.
- [34] J. Gascon, U. Aktay, M.D. Hernandez-Alonso, G.P.M. van Klink, F. Kapteijn, *J. Catal.* 261 (2009) 75–87.
- [35] N. Guillou, C. Livage, J. Chaigneau, G. F rey, *Powder Diffr.* 20 (2005) 288–293.
- [36] J. Yang, Q. Zhao, J. Li, J. Dong, *Microporous Mesoporous Mater.* 130 (2010) 174.
- [37] G. Tonetto, J. Atias, H. de Lasa, *Appl. Catal., A* 270 (2004) 9–25.
- [38] D. Do, *Adsorption Analysis: Equilibria and Kinetics*, Imperial College Press, London, 1998.
- [39] P.I. Ravikovitch, A.V. Neimark, *Langmuir* 18 (2002) 9830–9837.
- [40] T.V. Vu, H. Kosslick, A. Schulz, J. Harloff, E. Paetzold, H. Lund, U. Kragl, M. Schneider, G. Fulda, *Microporous Mesoporous Mater.* 154 (2012) 100–106.
- [41] M.J. Ingleson, J. Perez Barrio, J.-B. Guilbaud, Y.Z. Khimyak, M.J. Rosseinsky, *Chem. Commun.* (2008) 2680–2682.
- [42] H. Yim, E. Kang, J. Kim, *Bull. Korean Chem. Soc.* 31 (2010) 1041–1042.
- [43] Z. Wang, S.M. Cohen, *Angew. Chem.* 120 (2008) 4777–4780.